Materials Views
www.MaterialsViews.com

ADVANCED FUNCTIONAL MATERIALS
www.afm-journal.de

FULL PAPER

Dynamic Processes in Sandwich Polymer Light-Emitting Electrochemical Cells

Stephan van Reenen, René A. J. Janssen, and Martijn Kemerink*

The operational mechanism of polymer light-emitting electrochemical cells (LECs) in sandwich geometry is studied by admittance spectroscopy in combination with numerical modeling. At bias voltages below the bandgap of the semiconducting polymer, this allows the determination of the dielectric constant of the active layer, the conductivity of mobile ions, and the thickness of the electric double layers. At bias voltages above the bandgap, p–n junction formation gives rise to an increase in capacitance at intermediate frequencies (≈10 kHz). The time and voltage dependence of this junction are successfully studied and modeled. It is shown that impedance measurements cannot be used to determine the junction width. Instead, the capacitance at intermediate biases corresponds to a low-conductivity region that can be significantly wider than the recombination zone. Finally, the long settling time of sandwich polymer LECs is shown to be due to a slow process of dissociation of salt molecules that continues after the light-emitting p–n junction has formed. This implies that in order to significantly decrease the response-time of LECs an electrolyte/salt combination with a minimal ion binding energy must be used.

1. Introduction

The light-emitting electrochemical cell (LEC)[1] is a promising candidate for organic lighting applications as it can be completely processed from solution. In between the anode and the cathode only one layer needs to be deposited, which–ideally during operation transforms into five different layers with different properties and functions, see also **Figure 1**:[2–6] i) next to the anode and cathode electric double layers (EDLs) are formed to enhance injection; ii) adjacent to these EDLs, p- and n-type doped regions are formed to enhance carrier transport towards the iii) central undoped region where the carriers meet, form excitons, and recombine, resulting in the emission of light. The injection enhancement by EDL formation enables the use of solution-based high-workfunction electrodes, like PEDOT:PSS, without compromising electron injection or device performance.[7,8] The relative insensitivity to electrode material in combination with the single layer structure, potentially make LECs an excellent choice for low-cost solution-based organic lighting. However, at present, issues like a relatively short lifetime and a long turn-on time prevent widespread application; recent findings[4,5,9] suggest, however, that these issues are not fundamental and can be overcome by improved materials and device design.[10–14] The latter is impeded by a limited quantitative understanding of the LEC device physics.

Recently numerical modeling of planar LECs in combination with experimental work has shed some light on the operational mechanisms of LECs.[4,9,15,16] The planar structure of LECs is enabled by the highly conductive doped regions, which allow active layer thicknesses of over hundreds of micrometers. In these planar cells we have shown that their operation mode is strongly dependent on the ability to form Ohmic contacts by EDL formation.[4] Planar LECs follow the electrochemical doping model, as described above, when there is no injection limitation after EDL formation. If injection limitations remain present, thin sheets of uncompensated ions form close to the electrodes, generating relatively large fields that enhance injection as far as possible, leading to the (undesired) electrodynamic operation mode. However, in well-functioning devices, the potential drop over these EDLs should be similar to the injection barrier for carriers from the metal to the highest occupied molecular orbital (HOMO) or lowest unoccupied molecular orbital (LUMO) of the conjugated polymer. In case the LEC is able to form Ohmic contacts, it also forms doped transport regions by electrochemical doping of the conjugated polymer. This electrochemical doping consists of the stabilization of a positive or negative charge on the conjugated polymer by an oppositely charged ion. The amount of doping in planar cells was shown to be dependent on the total amount of salt added to the active layer.[9] Another study[5] on planar cells has shown that this electrochemical doping results in a strong increase in carrier mobility in the doped regions. Consequently there is a large conductivity difference between the doped regions and the intrinsic recombination region. This difference in conductivity leads to a relatively large potential drop over the recombination zone (Figure 1). Accordingly current conservation is obeyed.

These results are however all based on planar LECs in which scanning Kelvin probe microscopy could be used to visualize the characteristic potential shape[2,4,17,18] LECs that are relevant for practical use have a stacked structure, in which the active layer thickness is only a few hundreds of nanometers. This thickness difference forbids the direct translation of the electrochemical doping model from planar LECs to stacked LECs

S. van Reenen, Prof. R. A. J. Janssen, Dr. M. Kemerink
Department of Applied Physics
Eindhoven University of Technology
PO Box 513, 5600 MB, Eindhoven, The Netherlands
E-mail: m.kemerink@tue.nl

DOI: 10.1002/adfm.201200880

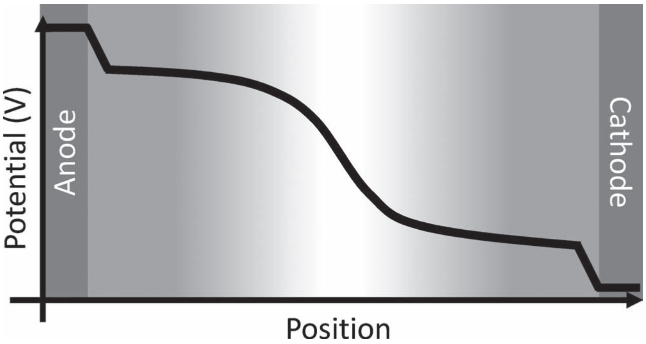

Figure 1. Schematic representation of the operation mechanism of the light-emitting electrochemical cell according to the electrochemical doping model.[3] The potential profile is plotted across the device with in the background the doping density. The darkness of the background scales with the density of the doping. The recombination zone is situated in between the doped regions at the large potential drop.

by simply reducing the thicknesses of the different regions. For instance, the recombination zone width found in planar LECs typically exceeds the layer thickness of stacked LECs.[18] One method to study the operation mechanism in stacked LECs is impedance spectroscopy. As this method uses a time-dependent signal, it is possible to look separately at fast and slow processes in LECs. This makes impedance spectroscopy potentially an excellent technique to disentangle the various ongoing processes in operational LECs.[6,19–24] However, the data generated by this technique is generally rather complicated and difficult to interpret. The work done on impedance spectroscopy in LECs has so far mainly focused on the junction width during operation. In polymer LECs junction widths between 10% and 80% of the active layer have been reported.[19,23] Furthermore, previous modeling studies to LECs were limited to steady-state.[4,9,25–28] Recently a study on sandwich LECs was published by Munar et al. in which equivalent circuit modeling was used to shed light on the LEC impedance spectrum.[29] However, interpretation of such modeling results is complicated by the sometimes intransparent physical meaning of the components. In particular, (combinations of) space charge and transit time effects tend to give rise to “inductive” responses that are hard to capture in equivalent RC networks.[19,34]

Here we combine impedance spectroscopy with numerical drift-diffusion modeling of polymer light-emitting electrochemical cells in stacked or sandwich geometry. We demonstrate that the observations are fully consistent with the above described electrochemical picture (see Figure 1) that was originally proposed for stacked devices[3] but so far only univocally confirmed for planar devices.[2,4] Information regarding the EDLs, ion conduction and the junction region is then obtained. Furthermore, our results show that the width of the recombination region cannot be simply extracted from the intermediate- or high-frequency capacitance: there is no abrupt transition from the doped regions to the intrinsic recombination region. The doping close to the junction region is not as dense as it is near the contacts. This can lead to a conductivity difference of a factor >10 throughout the doped regions. Moreover, we identify the dissociation of salt molecules into anions and cations as the slow process that is responsible for the characteristic long settling time of LECs.

2. Results and Discussion

Complex admittance measurements were performed on sandwiched polymer LECs. The complex admittance $\hat{Y}$ can be decomposed in a real part, the conductance G, and an imaginary part, which is proportional to the capacitance C. Both C and G typically depend on the angular frequency ω:

$$\hat{Y} = \frac{I_{\mathrm{ac}}}{V_{\mathrm{ac}}} = G(\omega) + i\omega C(\omega) \tag{1}$$

where I_{ac} and V_{ac} are the AC current and voltage signal, respectively.

2.1. Below-Bandgap Biases

Figure 2 shows the experimental and modeling results for LECs biased at 0 V. Figure 2a shows the conductance and capacitance

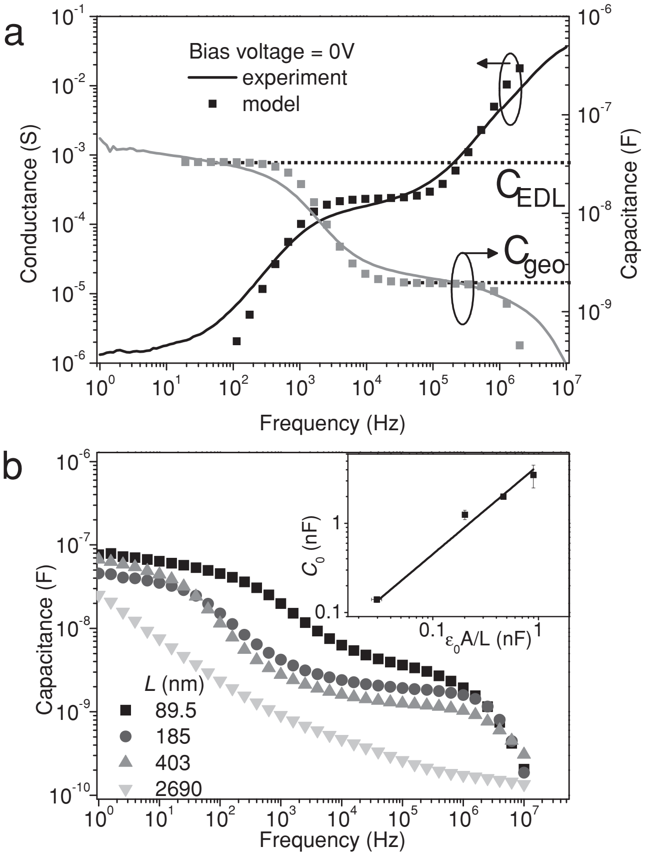

Figure 2. a) Conductance (black) and capacitance (gray) spectra of an MDMO-PPV at 0 V determined experimentally and by the numerical model. b) Measured capacitance spectra of MDMO-PPV LECs with different thicknesses. The inset shows the geometric capacitance (taken as C at 0.1 MHz) as a function of device length to determine the dielectric constant: $\varepsilon_r = 4.5 \pm 0.3$.

in LECs biased at 0 V as a function of frequency. The device under test is a pristine device, i.e., it has not been biased before. Therefore, only ions are present in the active layer and the presence of a significant amount of electronic carriers can be excluded. At high frequencies (>1 MHz) the conductance shows f^2 dependence which results from the displacement current.[19] At longer timescales a conductivity plateau (≈10 kHz) is observed which is related to ion transport. At these frequencies the geometric capacitance, C_{geo}, is observed, being approximately 2 nF. Moving towards lower frequencies, an increase in capacitance is observed. This increase is related to the formation of electric double layers (EDLs). At these low frequencies (≈10 Hz) the ions apparently have enough time to move towards the electrode interfaces where they are blocked. This results in the formation of EDLs, which resultantly remove the field in the bulk region. Consequently, the conductance starts to decrease at the same time scale at which EDLs start to form. The second conductance plateau (≈1 Hz) is related to leakage current. A modeling result of the conductance and capacitance spectra is shown in Figure 2a as well, showing good agreement with the experiments. A total of 0.5 V drops over the active layer because of the built-in voltage. The latter results from the choice of electrode work functions. After EDL formation the potential drops only at the electrode interfaces leaving the bulk field-free.

To obtain information about the EDLs in these devices, first the dielectric constant must be determined. This was done by measurement of the capacitance spectrum of LECs with different active layer thicknesses, L, as shown in Figure 2b. Here it is clear that the high frequency (≈0.1 MHz) the geometric capacitance decreases with increasing thickness. Furthermore it is observed that the low frequency (≈10 Hz) capacitance is not highly affected by a change of L. The inset of Figure 2b shows C_{geo} as a function of $\varepsilon_0 A/L$, such that the slope of the fitted line equals the relative dielectric constant, ε_r, of the layer. Here it is assumed that the LEC behaves like a parallel plate capacitor at high frequencies. ε_r is then determined to be 4.5 ± 0.3. This value was used for the modeling results shown in Figure 2a.

Now ε_r is known it is possible to obtain information about the EDLs shown in **Table 1**. It is assumed that the capacitance of both EDLs, C_{EDL}, is more or less similar. Both capacitances are connected in series such that the EDL with the smallest capacitance, i.e., the thickest EDL, is dominant. The thickness of the EDLs L_{EDL} can then be approximated as $L_{\text{EDL}}C_{\text{EDL}} = LC_{\text{geo}}$ must hold. The layer in between the sheet of ions and the electrodes is assumed to have the same dielectric constant as the rest of the film. From the experiment this procedure yields an EDL thickness of 5.4 ± 1.7 nm and from the model 5.87 nm. Note that this is the same as the width over which the potential drops at the contacts shown in Figure 1. From C_{EDL} also the charge density n per unit voltage can be calculated that drops over the EDL: $n/V = C/(qAL)$, where q is the elementary charge. A value of 0.007 and 0.009 $\text{nm}^{-3}\,\text{V}^{-1}$ is determined for the model and experiment, respectively. In the simulations, this value can also independently be determined from the anion and cation density difference near the electrodes. The potential drop over the electrodes is expected to become no more than 2 V during operation. Such a potential drop corresponds to a density of uncompensated ions of ≈$16 \times 10^{-3}\,\text{nm}^{-3}\,\text{V}^{-1}$. Such a density is only a small fraction of the average ion density, i.e., 0.1 nm^{-3}. This means that EDL formation to overcome injection barriers of even 2 V should not be problematic as sufficient ions are present in the active layer and that the thickness of the EDL is hardly affected by the actual potential drop over the EDLs. In general the model and experiment are in good agreement with each other (see Figure 2a and Table 1), suggesting that the described methods to determine both the ion density in the EDLs and the EDL thickness are valid.

Table 1. Electric double layer properties from model and experiment.

	Model	Experiment
C_{EDL} [nF]	66.1	70 ± 8
C_{geo} [nF]	1.94	1.9 ± 0.2
L [nm]	200	200 ± 10
L_{EDL} [nm] (calculated)	5.87	5.4 ± 1.7
Figure 2b: L_{EDL} [nm] (measured)	6.00	–
n/V [nm^{-3}] (calculated)	0.0070	0.0089 ± 0.001
Figure 2b: n/V [nm^{-3}] (measured)	0.0050	–

The effect of a larger potential drop over the EDLs was studied by measurement of the capacitance spectra at different bias voltages below the bandgap of the polymer. These results are shown in **Figure 3**a. Clearly C_{EDL} is not affected by a different V_{dc}, which corroborates the conclusion above that the density of ions in the EDL is small compared to the average ion density in the film. In the model the same result is obtained as shown in the inset. The effect of an elevated temperature was determined as well in Figure 3b. Here it is observed that C_{EDL} remains approximately constant when the temperature remains below the melting point (≈60 °C) of the PEO. Close to this melting point the capacitance increases by a small fraction, indicating a decrease of the EDL thickness. This can be rationalized by assuming that ions can move more easily through the 'molten' PEO towards the electrode. After this the temperature was reduced and the former C_{EDL} was retrieved. The higher temperature clearly did not result in an irreversible change in the formation of EDLs. The frequency at which C_{EDL} transfers into C_{geo} will be discussed below.

The results shown in Figure 2a also give information about the ion conductivity, next to the already discussed dielectric constant and EDLs. First of all the presence of a conductance plateau (at ≈10 kHz) indicates that at least a part of the salt is dissociated in the active layer, most likely in the PEO phase. The plateau value of the conductance can be used to determine the total conductivity of the ions, σ, in the active layer by

$$\sigma = q\,(\mu_a + \mu_c)\,c_0 = \frac{GL}{A} \tag{2}$$

where μ_a and μ_c are the anion and cation mobility respectively and c_0 is the ion density. Extracted values for $(\mu_a + \mu_c)c_0$, which in turn can be used to make an estimate of the sum of the anion and cation mobilities, are shown in **Table 2**. This is done by a simple division by the ion density. For the model a similar value for the ion mobility is retrieved as was initially put into the simulation. For the experiment only a lower limit of the summed

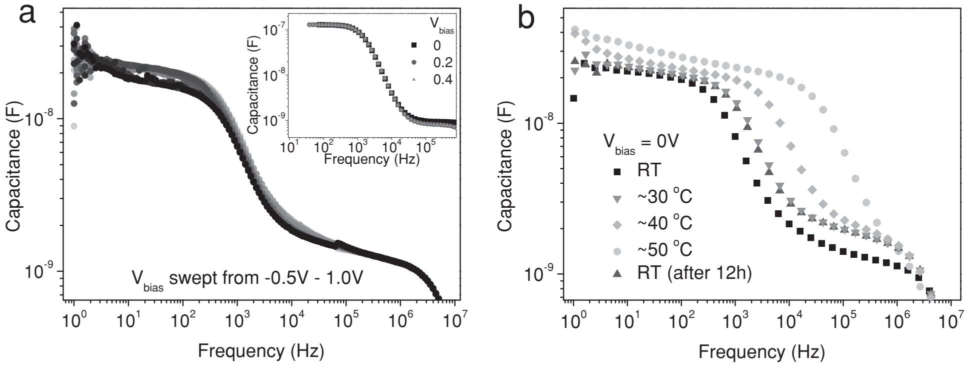

Figure 3. Electric double layer capacitance at a) different bias voltages below the bandgap and b) different temperatures. The inset in (a) shows the modeling of the EDL capacitance at different voltages.

mobility can be determined as the amount of mobile ions has not been determined. From this follows a summed mobility of 10^{-13} m^2 $V^{-1}s$ $^{-1}$. Unfortunately, admittance measurements cannot be used for independent determination of the ion density and ion mobility. Aggregation of anions and cations as well as a difference in anion and cation density has furthermore not been taken into account and is subject of further study.

Temperature dependent measurements of the conductivity are shown in **Figure 4**, represented as a loss-frequency plots. The loss is determined by of the ratio of the conductance and the frequency of the AC signal at which it was measured. A strong dependence on temperature is found. The first measurement at room temperature shows a clear peak at 10^3 Hz. Subsequent measurements show a strong increase at low frequency which is attributed to leakage (c.f. Figure 2a). Therefore the other peaks become shoulders on the larger leakage peak; the effect of the temperature on the conductance is nevertheless still clear. The loss peak moves towards higher frequencies for higher temperatures whereas the peak height remains constant. At ≈50 °C the ion conductance has increased by 2 decades as compared to RT. Similar temperature effects on the conductivity have been reported by Torell et al.[32] on PEO-based $NaCF_3SO_3$ polymer electrolytes. In particular, they showed that mainly the mobility is affected by a change in temperature, whereas the ion density even slightly decreases at higher temperatures. Combined with the results in Figure 4a this indicates that the ion mobility in LECs is strongly temperature dependent. In Figure 4b modeling results are shown to study the effect of the ion mobility and mobile ion density on the loss spectrum of the LEC. In line with the preceding discussion, the calculated loss spectrum moves to higher frequencies without substantial changes in peak height for increasing ion mobility. Reduction or increase of the mobile ion density has a less pronounced effect on the peak position, and does strongly affect the loss peak height. In the experiment the peak height is observed to be constant.

Table 2. Ion conductivity properties extracted from model and experiment.

	Model	Experiment
G [S]	$2.36 \cdot 10^{-4}$	$(2.2 \pm 1.0) \times 10^{-4}$
L [nm]	200	200 ± 10
A [cm^2]	0.091	0.091
Equation (2): $q\mu_a + \mu_c c_0$ [V^{-1} s^{-1} m^{-1}]	5.2×10^{-6}	$(4.8 \pm 2.0) \times 10^{-6}$
c_0 [nm^{-3}]	0.1	0.3
$\mu_a + \mu_c$ [m^2 V^{-1} s^{-1}] (calculated)	3.04×10^{-13}	$(1.0 \pm 0.6) \times 10^{-13}$
$\mu_a + \mu_c$ [m^2 V^{-1} s^{-1}] (measured)	2.92×10^{-13}	–

2.2. Above-Bandgap Biases

Complex admittance spectra of a typical MDMO-PPV/PEO/KCF_3SO_3 LEC at multiple bias voltages are shown in **Figure 5**. Already at $V_{bias} = 2$ V the admittance spectra start to differ from the 0 V measurement, indicating the onset of charge injection and doping. At larger bias voltages ($V_{bias} > 2$ V) the high frequency capacitance increases, which below will be related to the formation of highly conductive doped regions. Towards lower frequencies a change of sign is observed in the capacitance.[19] The cross-over to this negative capacitance (NC) moves to higher frequencies for increasing bias voltage. Its position stabilizes near 1 kHz. The NC dominates the rest of the low frequency capacitance.

In the conductance spectrum a relatively high conductance is observed at high frequencies (≈1 MHz). This conductance decreases when the frequency of the driving signal is decreased and is accompanied by an increase in the capacitance. This behavior can be explained by the presence of highly conductive regions near the electrodes that sandwich a less conductive region as sketched in Figure 1: At the highest frequencies the distance the electronic charge carriers can travel is short in comparison to all other length scales in the device, hence all carriers can contribute to the conductance. Upon reducing the frequency, this distance increases and consequently carriers will start to enter regions of lower density/conductance, causing a) a reduction in conductivity and b) a pile-up of charges; which is reflected in an increasing capacitance. In reality the density and conductivity vary gradually throughout the doped regions,

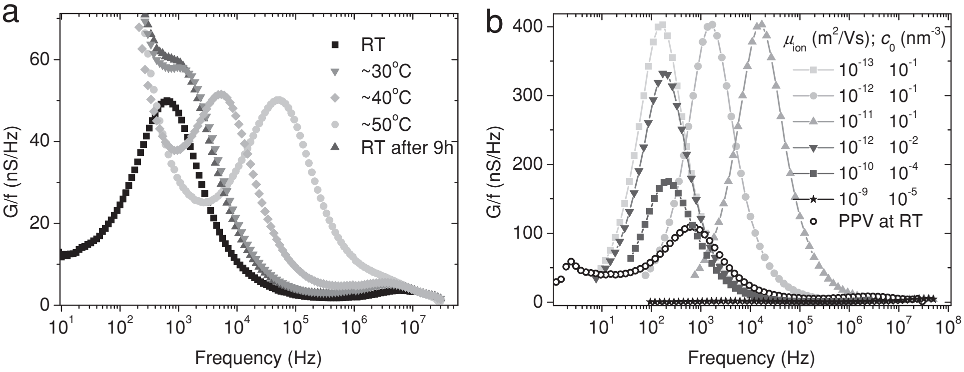

Figure 4. a) The loss (i.e.; conductance/frequency) in MDMO-PPV LECs at different temperatures. b) Modeled effect of ion mobility and ion density on the loss spectrum in LECs.

causing also the changes in C (ω) and G (ω) to be gradual. The maximum capacitance (≈10 kHz) is then related to the capacitance of the junction region. From this maximum capacitance the junction width was determined by the same procedure as shown e.g., in ref. [19,20,23]. Below however we show that the width determined from this capacitance is not a correct estimate of the width of the light-emitting p-n junction. Concomitantly, the corresponding conductance at these intermediate frequencies is related to the conductance in the low-conductive region of the cell, i.e., the p-n junction. Moving towards lower frequencies, the conductance is observed to increase again. This increase coincides with the NC observed in the capacitance plots.

Further admittance measurements were taken on nominally identical pristine LECs at 10 kHz to study the time- and voltage-dependence of the low-conductivity region. In **Figure 6** typical results are shown for MDMO-PPV LECs and SY-PPV LECs. The junction width was estimated from the measured capacitance by approximating the junction region by a parallel plate capacitor with area $A = 0.091$ cm^2. First the settling time of the capacitance was measured after application of 3.5 V (see Figure 6a,b). For the MDMO-PPV device the capacitance increases to a maximum within a few seconds. Initially the geometric capacitance was obtained, i.e., 3.6 nF, after which it peaks at 6.3 nF in 5 s. After that the capacitance slowly decreases. Simultaneously, the current, and hence the conductance, increase monotonously. The combination of capacitance and conductance in time show that junction formation is relatively fast <2 s, and is followed by a relatively slow doping process that takes approximately a minute to come close to settling. For the SY-PPV LEC a similar result is observed. Differences are a faster settling time for SY-PPV and a decreasing junction width during doping maximization.

Measurements of the 10 kHz capacitance and conductance were also performed at different bias voltages as shown in Figure 6c,d for MDMO-PPV and SY-PPV LECs, respectively. Pristine LECs were used. At each bias voltage the device was allowed to settle for at least 3 min. The capacitance of the MDMO-PPV LEC (see Figure 6c) increases sharply between 2.5 and 3 V, reaching a maximum value of ≈9 nF at 3 V. The increase of the capacitance can be explained by the progressive formation of doped regions starting at the electrodes. Consequently, a central low-conductivity region remains which leads to an increase in the capacitance above the geometric capacitance of the device. Apparently the increase of voltage between 2.5 V and 3.0 V leads to a strong enhancement of the doping.

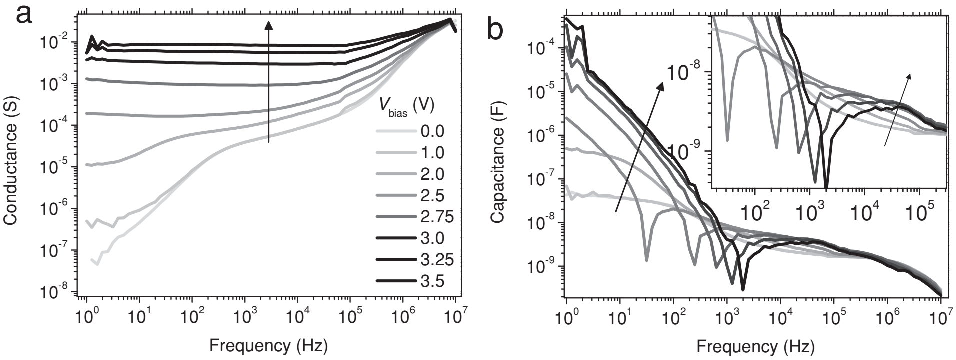

Figure 5. The a) conductance and b) capacitance spectra of an MDMO-PPV/PEO/KCF$_3$SO$_3$ LEC at different bias voltages. The inset in (b) shows the high-frequency part of the capacitance in more detail. Measurements were taken upward in voltage.

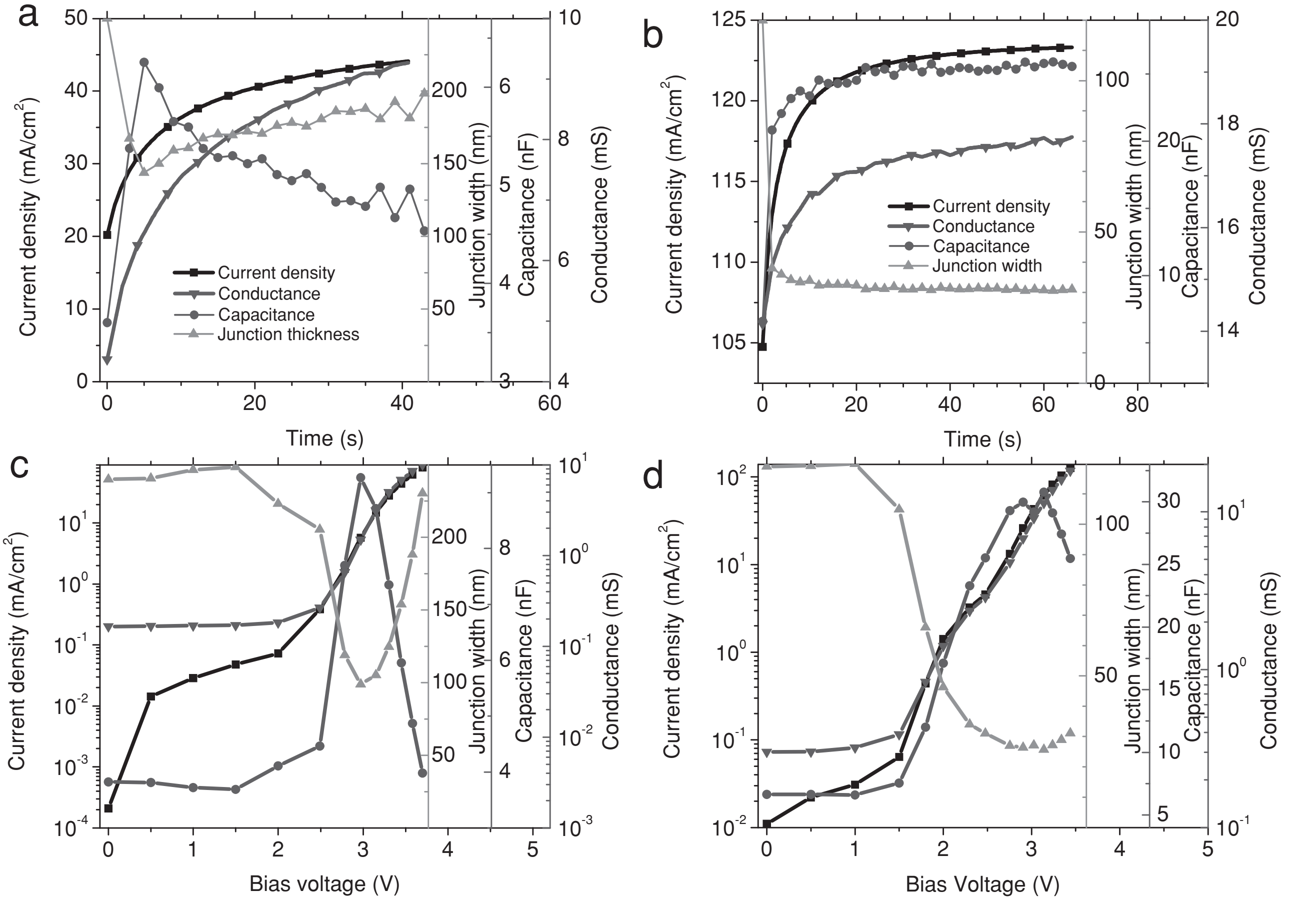

Figure 6. Electrical characterization as a function of a,b) time and c,d) voltage for a,c) MDMO-PPV LECs and b,d) SY-PPV LECs.

This is also visible in the strongly increasing conductance and current. Above 3.0 V the capacitance decreases again, indicating that the doped regions shrink. This can be explained by current conservation and exhaustion of paired mobile ions, i.e., salt. The increase in voltage leads to an increase in field in the junction region. This field would significantly increase the current density through the junction region if its width remained constant. However, since the conductivity of the doped regions cannot be increased further because of the exhaustion of salt, the current is limited and the junction region needs to become wider again. Concomitantly the doped regions become more compact, creating a larger doping density in a smaller region. Note that in the same voltage range, current and conductance do show a net increase. Qualitatively similar behavior is observed for the SY-PPV LEC in Figure 6d. Differences between SY-PPV LECs and MDMO-PPV LECs are likely related to differences in the doping- and field-dependence of the carrier mobilities. Also the salt binding may be affected by the use of different (batches of) polymers. All these effects will be discussed below.

Next to electrical characterization of the LECs, also optical measurements were performed. The results hereof are presented in the Supporting Information and are in full agreement with previously reported results.[6] However, the trends of the luminance and efficacy measured as a function of time and voltage showed no relevant correlation with the trends in the junction width as determined from the high frequency capacitance.

An interesting comparison between different device configurations can however be made. The width of the recombination zone in a planar polymer LEC (interelectrode distance of 35 μm) was previously found to be between 3 to 6 μm: a junction width to active layer thickness ratio of ≈0.1.[18] The measurements presented here have shown that for sandwich LECs this ratio can vary between 0.3 and 0.8. Clearly scaling down of the LEC increases the relative width of the recombination zone although the absolute width decreases significantly.

To further understand the admittance results shown in Figure 5 and 6, the model was used to calculate both transient and steady-state properties of LECs. In **Figure 7**a modeled current transients are shown using the parameters given in the methods section. The bias voltage that is applied to the 200 nm LEC is 3.5 V. The ion mobility was set at 10^{-13} m^2 V^{-1} s^{-1} to speed up calculations. The ion mobility is at least a factor of 10 smaller than the slowest electron or hole in the device. Simulations were done with and without a binding energy between the paired anions and cations, i.e., the neutral salt, to

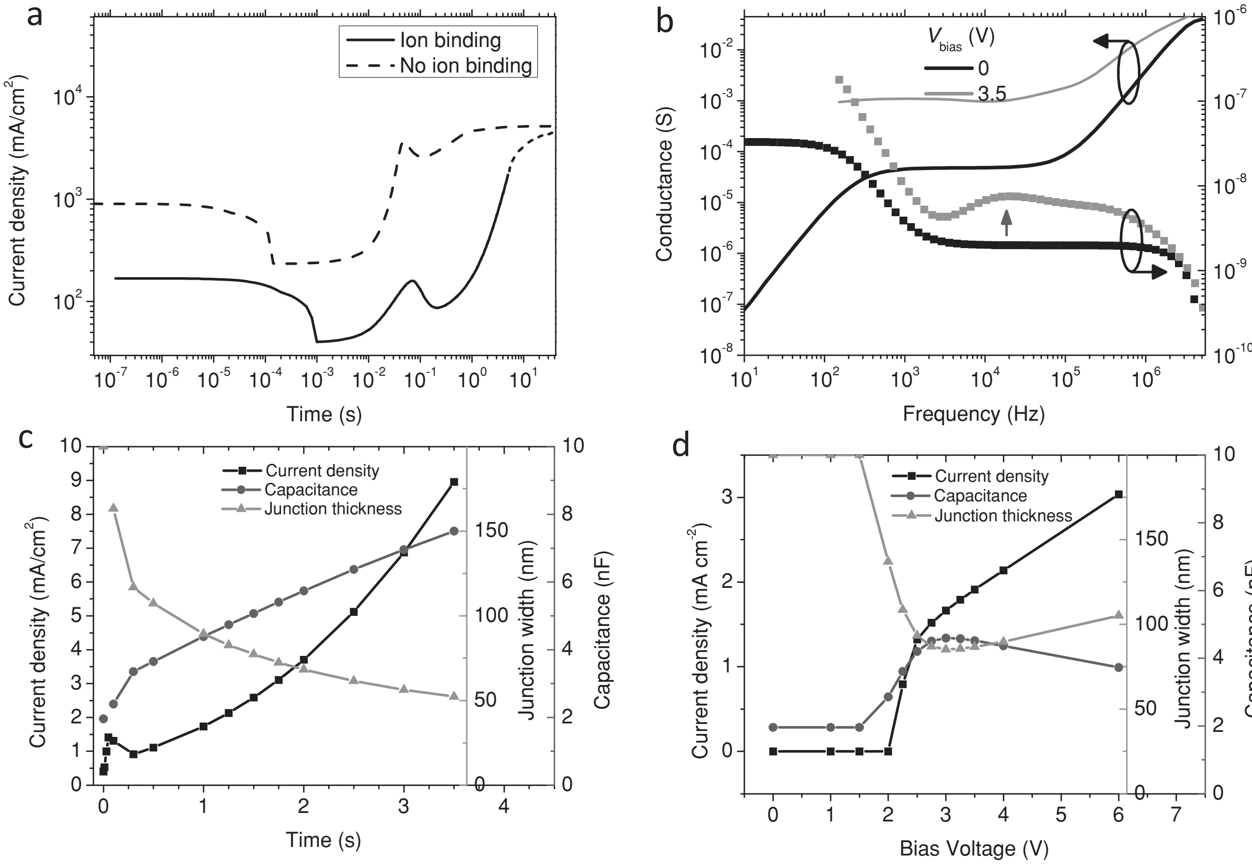

Figure 7. Modeling results of a 200 nm LEC with a surface area of 0.1 cm^2. a) Current transients for an LEC with and without binding energy between the cations and anions. The dotted line indicates the continuing trend. b) Typical high frequency impedance spectra. The vertical arrow denotes the peak position used for junction width determination. c) Electric characterization as a function of time at 3.5 V. d) Electric characterization as a function of voltage after 1.0 s.

study its effect on the current transients. At the shortest times in Figure 7a ($t < 10^{-3}$ s) the current is solely carried by ions, forming EDLs. During EDL formation the current drops ($10^{-4} < t < 10^{-3}$) due to screening of the electric field by the EDLs. At the same time injection and doping are initiated. The results both show junction formation at around 10^{-1} s, highlighted by a peak in the current. The junction formation time is not related to the ion conductivity, but seems solely related to the mobility of the ions, which is the same for both current transients in Figure 7a. The mobile ion density differs by a factor of 10 as does the ion conductivity. After junction formation both simulations start to qualitatively differ. In case no binding energy is present, the current relaxes towards a steady-state value. This behavior was also observed and modeled in wide interelectrode gap LECs.[4] In case a salt binding energy is present, a large fraction of the ions cannot immediately be used for doping. The salt however slowly dissociates over time because of the depletion of free anions and cations from the n- and p-doped regions, respectively. As a result, the current increases over a long time span. The same was observed in Figure 6a,b, where relatively fast junction formation was followed by a slow increase of the current. Because of long calculation times, it is not feasible to calculate the complete transient for a time span of 50 s and only the first few seconds have been modeled. In either case, the long turn-on time in LECs can now be directly related to the binding energy between the anions and the cations; junction formation itself is a relatively fast process that occurs within a second. The experimental time resolution was insufficient to observe sub-second transient features.

Typical admittance spectra of modeled LECs are shown in Figure 7b. The increased capacitance at high frequencies (>1 kHz) as well as the behavior of the conductance are qualitatively similar in the experiment and the model. One major difference however is the strong positive capacitance at low frequencies (<1 kHz) encountered in the modeling result, whereas a negative capacitance is observed in the experiment (see Figure 5b). We will come back to this discrepancy at the end of this section. To show that the intermediate- and high-frequency part of the spectrum is correctly modeled and interpreted, similar experiments were done in the model as were done in the experiments (Figure 6). In Figure 7c the time evolution of the capacitance at 10 kHz is shown. Initially, at $t = 0$ s the geometric capacitance is obtained. After that the junction forms within 0.1 s, as shown in Figure 7a. Necessarily doping of the active layer has then also started, but complete doping is delayed by the dissociation-limiting binding energy. The timescale of the process

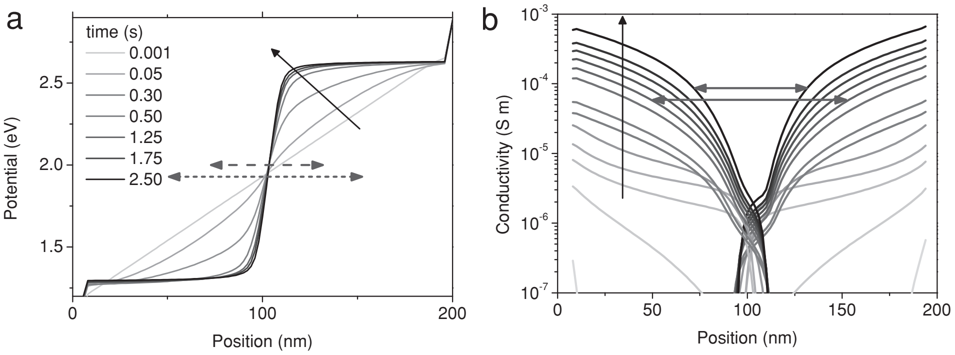

Figure 8. Modeling results of a 200 nm LEC with a surface area of 0.1 cm^2. a) Potential and b) carrier conductivity profile evolution corresponding to results shown in Figure 7c.

modeled here is mostly related to the binding-debinding of the salt and the related doping process; the mobility of the carriers is not limiting the evolution of the LEC as follows from the fast (<0.1 s) junction formation. Like for panel a, the modeling results in panel c are qualitatively similar to the experiments in Figure 6a,b. The high capacitance due to the low-conductivity region forms within 2 s and is then nearly saturated. The current density however has not and will continue to increase for a much longer time: dissociation of the salt is on-going. The voltage dependence of the capacitance is plotted in Figure 7d. Again a qualitatively similar result is obtained as in the experiment (Figure 6c,d). For above-bandgap (2.4 eV) voltages the junction has formed; its width decreases until 2.8 V and starts to increase again for larger bias voltages. The current however increases monotonously with increasing voltage. The doped regions are furthermore observed to become more narrow, resulting in an increase of conductance in the doped regions (see Supporting Information).

Figure 8a shows the potential profile of the modeled LEC after different times following the application of 3.5 V. In Figure 7c the junction width is plotted as well, determined by assuming the low-conductivity region can be described as a parallel plate capacitor. In Figure 8a this gap, ranging between ≈60 and ≈100 nm is compared to the potential drop over the recombination zone. They are not at all identical: there is a large mismatch, e.g., ≈60 nm vs. ≈20 nm for times longer than ≈1 s. In Figure 8b the electronic conductivity is plotted as a function of position. The conductivity is determined by multiplication of the carrier density, the (local field and doping dependent) mobility and the elementary charge q. The conductivity is largest close to the electrodes and gradually decreases towards the recombination region in the center. The conductivity in the recombination zone ($90 < x < 110$ nm) is a factor 10^2 smaller compared to the average conductivity in the doped regions. Interestingly, the junction width as determined from the capacitance seems to be more related to the width of the low-conductivity region then to the width of the recombination region as estimated from the potential drop. The latter is also equal to the width of the recombination profile.

These findings indicate that the junction width as obtained from impedance measurements is determined by the mobility and density of electrons and holes throughout the device. The mobility is density[33] and field dependent, complicating things further. Also the recombination process has a large influence on the conductivity in the intrinsic region: a low recombination probability results in a larger space charge compensation, leading to larger carrier densities, hence a larger carrier conductivity. The high frequency capacitance is therefore only a measure for the conductance difference between the highly doped regions near the contacts and the less conductive central region. Examples of LECs in which the doping and field dependencies of the mobility were altered are shown in the Supporting Information. All these effects may explain the wide range of reported junction widths obtained by admittance measurements.[19,20,23]

The only part of the admittance measurements that is presently not understood is the negative capacitance (NC) at $V_{\text{bias}} > E_{\text{g}}$ below 1 kHz (Figure 5b). A similar NC was reported before in ref. [19]. The measurements show that the process related to this negative capacitance is reversible and continuous below 1 kHz. Carrier traps in the doped or intrinsic region were introduced in the model but did not result in an NC. Alternatively, one might associate the NC with space charge compensation effects as known in conventional bipolar diodes,[34] especially since space charge limited behavior has been observed in LECs.[6] Also this scenario seems unlikely as the model does reproduce the pronounced NC behavior for bipolar diodes without ions/salt. The fact that the model cannot reproduce the low-frequency NC indicates that the numerical model, and our understanding of LECs, is not yet complete.

3. Conclusions

Admittance spectroscopy proves valuable to gain more information on the operational mechanism of polymer LECs in stacked or sandwich geometry. The obtained results were successfully modeled and can be interpreted according to the electrochemical doping model.[3] Measurements where the bias voltage does not exceed the bandgap enabled determination of the electric double layer thickness and of the conductivity of the mobile ions. Measurements in which the bias voltage exceeds the bandgap, enabled the identification of a low-conductivity junction region sandwiched by high-conductivity doped regions. Modeling of LECs has, counter intuitively, shown that the low-conductivity region is not similar in width as the recombination zone. Finally, the relatively large turn-on time in LECs, typically in the order of seconds, was found to be unrelated to the low ion mobility, but rather to be due to the binding energy between anions and cations.

4. Experimental Section

Device Preparation: For the conjugated polymer in the active layer of our sandwich LECs either poly[2-methoxy-5-(3′,7′-dimethyloctyloxy)-p-phenylene vinylene] (MDMO-PPV, $M_w > 1 \times 10^6$ g mol^{-1}, American Dye Source) or a phenyl-substituted poly(p-phenylene vinylene) copolymer (SY-PPV, Merck, catalogue number PDY-132), commonly termed "superyellow" was used. Poly(ethylene oxide) (PEO, $M_w = 5 \times 10^5$ g mol^{-1}, Aldrich) was used as received. PL and EL spectra of the devices are shown in the Supporting Information. The salt potassium trifluoromethanesulfonate (KCF_3SO_3, 98%, Aldrich) was dried at 473 K under vacuum before use. MDMO-PPV (10 mg mL^{-1}) and SY-PPV (5 mg mL^{-1}) were dissolved in chloroform (>99%, anhydrous, Aldrich). PEO and KCF_3SO_3 were dissolved separately (10 mg mL^{-1}) in cyclohexanone (>99%, anhydrous, Aldrich). These solutions were mixed together in a weight ratio of PPV/PEO/KCF_3SO_3 = 1:1.35:0.25. These blend solutions were thereafter stirred on a magnetic hot plate at a temperature $T = 323$ K for 5 h.

ITO patterned substrates were spin-coated with the blend solution at 800 rpm for 60 s, followed by 1000 rpm for 10 s after which they were dried on a hot plate at $T = 323$ K for at least 1 h. The resulting active layer thickness was 200–250 nm for MDMO-PPV LECs and 100 nm for SY-PPV LECs, as determined by profilometry. Al electrodes were deposited by thermal evaporation under high vacuum on top of the spin-coated films. The final device area was 0.091 cm^2. All the above procedures, except for the cleaning of the substrates, were done in a glove box under N_2 atmosphere ($[O_2] < 1$ ppm and $[H_2O] < 1$ ppm) or in an integrated thermal evaporator.

Electrical Characterization: A Keithley 2636a sourcemeter was used to drive the devices and measure the current. The brightness was measured with a luminance meter (LS-110 Konica-Minolta). A Solartron 1260 was used to perform complex admittance measurements on the LECs in the glove box at room temperature. After applying a bias, cells were allowed to settle for 1 min before the admittance spectrum was measured. Each point (from 30 MHz to 1 Hz) was measured during an integration time of 1 s. The rms-value of the AC voltage was 0.01 V.

Computational Details: A 1D model[4] was used in which an active layer of length $L = 200$ nm was divided in $N = 99$ discrete points. The numerical model solves the drift-diffusion equations for electrons, holes, anions and cations, and Poisson's equation on this grid by forward integration in time. Devices with a bandgap $E_g = 2.4$ eV were simulated during operation at a given bias voltage V_{bias} until steady state had been reached, recognized by a zero ion current. A detailed description of the numerical model can be found in the Supporting Information. Simulations were run for devices with initial ion concentrations $c_0 = 0.1$ nm^{-3}. Unless stated otherwise, no binding energy was assumed between anions and cations. The electrodes were ionically-blocking and electrons and holes were injected from the contacts according to an empirical injection model that gives rise to field-dependent injection. This model is described in the Supporting Information and has the advantage that injection is not affected by grid-point spacing. The hole and electron injection barriers were set at 0.5 and 1.4 eV respectively to simulate an asymmetric device. Similar injection barriers are expected for PPV-type materials sandwiched between ITO and Al electrodes. Bimolecular electron-hole recombination was described as a Langevin process. The electrostatic potential was determined by Poisson's equation. In addition, we set the relative dielectric constant $\varepsilon = 4.5$ and the temperature $T = 300$ K. Energetic and spatial disorder in the system were implemented via the hole and electron mobilities that were described by a field- and density-dependent mobility model.[5] The field dependence is assumed to follow Poole-Frenkel behavior with exponential factor $\gamma = 2 \times 10^{-4}$ (m/V)$^{0.5}$.[30,31] A detailed description of the used density dependence of the mobility can be found in the Supporting Information. The carrier mobility in the absence of field and doping was $\mu_{p/n} = 1 \times 10^{-12}$ m^2 V^{-1} s^{-1}. The anion and cation mobilities were chosen to be $\mu_{ion} = 1 \times 10^{-13}$ m^2 V^{-1} s^{-1}. To model the admittance spectrum, the LEC was first allowed to reach steady-state. After this, a voltage step of 0.01 V was applied and the resulting step response of the current was calculated. The complex admittance spectra can then be derived by a fast Fourier transform of the derivative of the conductance. All simulations were started from a pristine device which only contains a homogeneously distributed amount of ions. After setting a specified bias voltage over the electrodes, the device was allowed to evolve in time, as determined by the processes described above. The parameters given above were used for all simulations presented in this paper, unless stated otherwise.

Supporting Information

Supporting Information is available from the Wiley Online Library or from the author.

Acknowledgements

The authors acknowledge financial support from the Dutch program NanoNextNL.

Received: March 28, 2012
Published online: June 25, 2012

---

[1] Q. B. Pei, G. Yu, C. Zhang, Y. Yang, A. J. Heeger, *Science* **1995**, *269*, 1086.
[2] P. Matyba, K. Maturova, M. Kemerink, N. D. Robinson, L. Edman, *Nat. Mater.* **2009**, *8*, 672.
[3] Q. B. Pei, Y. Yang, G. Yu, C. Zhang, A. J. Heeger, *J. Am. Chem. Soc.* **1996**, *118*, 3922.
[4] S. van Reenen, P. Matyba, A. Dzwilewski, R. A. J. Janssen, L. Edman, M. Kemerink, *J. Am. Chem. Soc.* **2010**, *132*, 13776.
[5] S. van Reenen, R. A. J. Janssen, M. Kemerink, *Org. Electron.* **2011**, *12*, 1746.
[6] M. Lenes, G. Garcia-Belmonte, D. Tordera, A. Pertegas, J. Bisquert, H. J. Bolink, *Adv. Funct. Mater.* **2011**, *21*, 1581.
[7] P. Matyba, H. Yamaguchi, G. Eda, M. Chhowalla, L. Edman, N. D. Robinson, *ACS Nano* **2010**, *4*, 637.
[8] P. Matyba, H. Yamaguchi, M. Chhowalla, N. D. Robinson, L. Edman, *ACS Nano* **2011**, *5*, 574.
[9] S. van Reenen, P. Matyba, A. Dzwilewski, R. A. J. Janssen, A. Edman, M. Kemerink, *Adv. Funct. Mater.* **2011**, *21*, 1795.
[10] C. V. Hoven, H. P. Wang, M. Elbing, L. Garner, D. Winkelhaus, G. C. Bazan, *Nat. Mater.* **2010**, *9*, 249.
[11] Z. B. Yu, M. L. Wang, G. T. Lei, J. Liu, L. Li, Q. B. Pei, *J. Phys. Chem. Lett.* **2011**, *2*, 367.
[12] S. Tang, L. Edman, *Electrochim. Acta* **2011**, *56*, 5.
[13] H. C. Su, H. F. Chen, Y. C. Shen, C. T. Liao, K. T. Wong, *J. Mater. Chem.* **2011**, *21*, 8.
[14] Z. Yu, M. Wang, G. Lei, J. Liu, L. Li, Q. Pei, *J. Phys. Chem. Lett.* **2011**, *2*, 6.
[15] K. O. Burnett, P. P. Crooker, N. M. Haegel, Y. Yoshioka, D. MacKenzie, *Synth. Met.* **2011**, *161*, 1496.

[16] J. Gao, Y. F. Hu, *J. Am. Chem. Soc.* **2011**, *133*, 2227.
[17] J. D. Slinker, J. A. DeFranco, M. J. Jaquith, W. R. Silveira, Y. W. Zhong, J. M. Moran-Mirabal, H. G. Craighead, H. D. Abruna, J. A. Marohn, G. G. Malliaras, *Nat. Mater.* **2007**, *6*, 894.
[18] D. B. Rodovsky, O. G. Reid, L. S. C. Pingree, D. S. Ginger, *ACS Nano* **2010**, *4*, 2673.
[19] G. Yu, Y. Cao, C. Zhang, Y. F. Li, J. Gao, A. J. Heeger, *Appl. Phys. Lett.* **1998**, *73*, 111.
[20] Y. F. Li, J. Gao, G. Yu, Y. Cao, A. J. Heeger, *Chem. Phys. Lett.* **1998**, *287*, 83.
[21] Y. F. Li, J. Gao, D. L. Wang, G. Yu, Y. Cao, A. J. Heeger, *Synth. Met.* **1998**, *97*, 191.
[22] J. Gao, A. J. Heeger, I. H. Campbell, D. L. Smith, *Phys. Rev. B* **1999**, *59*, R2482.
[23] I. H. Campbell, D. L. Smith, C. J. Neef, J. P. Ferraris, *Appl. Phys. Lett.* **1998**, *72*, 2565.
[24] M. Buda, G. Kalyuzhny, A. J. Bard, *J. Am. Chem. Soc.* **2002**, *124*, 6090.
[25] J. C. deMello, N. Tessler, S. C. Graham, R. H. Friend, *Phys. Rev. B* **1998**, *57*, 12951.
[26] J. C. deMello, J. J. M. Halls, S. C. Graham, N. Tessler, R. H. Friend, *Phys. Rev. Lett.* **2000**, *85*, 421.
[27] J. C. deMello, *Phys. Rev. B* **2002**, 66.
[28] D. L. Smith, *J. Appl. Phys.* **1997**, *81*, 2869.
[29] A. Munar, A. Sandström, S. Tang, L. Edman, *Adv. Funct. Mater.* **2012**, *22*, 1511.
[30] A. R. Buckley, *Synth. Met.* **2010**, *160*, 540.
[31] J. Frenkel, *Phys. Rev.* **1938**, *54*, 647.
[32] M. Kakihana, S. Schantz, L. M. Torell, *J. Chem. Phys.* **1990**, *92*, 6271.
[33] H. Shimotani, G. Diguet, Y. Iwasa, *Appl. Phys. Lett.* **2005**, *86*, 022104.
[34] H. H. P. Gommans, M. Kemerink, R. A. J. Janssen, *Phys. Rev. B* **2005**, 72.